Article

Effects of Electrolyte Compositions and Electrical Parameters on Micro-Arc Oxidation Coatings on 7075 Aluminum Alloy

Aqeel Abbas (ID)**, Ting-Yi Wang and Hsin-Chih Lin ***

Department of Materials Science and Engineering, National Taiwan University, Taipei 10617, Taiwan;
engr.aqeel14@gmail.com (A.A.)
* Correspondence: hclinntu@ntu.edu.tw

Abstract: Aluminum alloys are widely used in a variety of industries nowadays for their high strength-to-weight ratio, good formability, low density, and recyclability. However, their poor corrosion and wear resistance properties restrict their applications. This study investigated the effects of electrical parameters and electrolyte compositions on the microstructures of micro-arc oxidation (MAO) film on a 7075 Al alloy substrate. The morphology, microstructure, and compositions of the MAO coatings were characterized using a scanning electron microscope (SEM), X-ray diffraction (XRD), and an electron probe micro-analyzer (EPMA). Furthermore, measurements of microhardness, corrosion resistance, and wear resistance were also conducted. The cathodic current and duty ratio are proportional to film thickness, which consequently improves the wear and corrosion resistance. The microstructural observations of the aluminate-based coatings revealed that increasing cathodic current reduces the pancake-like structures, and a lot of small pores appear on the top of the coatings, which makes the surface smoother. Moreover, the aluminate-based coatings are mainly composed of α-Al$_2$O$_3$ and γ-Al$_2$O$_3$, while the silicate-based coatings mainly consist of γ-Al$_2$O$_3$ and a small amount of α-Al$_2$O$_3$ phase. Due to the phase compositions, the microhardness of the aluminate-based coatings can reach 1300~1500 HV and exhibit better wear resistance than silicate-based coatings.

Keywords: 7075 aluminum alloy; micro-arc oxidation; microstructure; corrosion resistance; wear resistance

1. Introduction

Aluminum is lightweight (density of 2.7 g/cm^3) and the third most abundant element in the earth's crust (after oxygen and silicon), and it ranks first among metals. It is widely used in household products, auto parts, aircraft parts, building materials, and general machinery parts because of its high specific strength, low price, good formability, and excellent electrical and thermal conductivity [1–3]. Although pure aluminum is light and has good corrosion resistance, its strength is insufficient. It cannot use phase transformation to improve its properties similar to steel because aluminum has no phase transformation in the solid state. Therefore, special alloying elements are often used to increase the strength of the aluminum alloy [4].

A stable and thin film with a thickness of about 2.5~10 nanometers is formed on the surface of pure aluminum when exposed to the atmosphere or water. The developed alumina film (Al$_2$O$_3$:3H$_2$O) prevents the surface from further oxidation and enhances corrosion resistance. It is stable in a neutral environment (pH range of 4~8.5) but will disintegrate if it exceeds this range [5,6].

Localized corrosion including pitting occurs on the surface when naturally formed dense passivation film is dissolved [7]. The corrosive ions are mainly halogen ions such as Cl$^-$, Br$^-$, and I$^-$, and these ions often attack the weak areas of the oxide film. The negatively charged chloride ions will be attracted to pits in order to maintain balance, which accelerates the rate of pitting corrosion and makes it more difficult to repair aluminum alloys [8,9].

Aluminum alloy surfaces can be modified using thermal, chemical, electrochemical, and other methods, such as physical vapor deposition (PVD), chemical vapor deposition (CVD), cold spraying (CS), laser surface modification, chemical conversion coating, electroplating, anodizing, hard anodizing (HA), and micro-arc oxidation [10]. Micro-arc oxidation (MAO) is an emerging electrochemical surface treatment technology for forming an oxide ceramic film on the surface of light metals [11]. MAO coatings have excellent properties of thermal stability, wear resistance, and high hardness. However, the porous and coarse nature of the film reduces corrosion and tribological resistance [12,13]. The film properties and morphology are directly related to growth mechanisms. It has been established by many researchers that MAO coatings grow inward from the substrate, leading to an increase in film thickness and a decrease in substrate thickness [14–16]. The phenomenon relies on the inward movement of oxygen atoms and interacts with the surface of the substrate, and the discharge channel model explains the process. The higher thickness of the film leads to improved corrosion resistance. Jian Chen et al. [17] prepared a self-lubricating composite coating on 6061 aluminum alloy using MAO technology and concluded that micropores are effectively sealed and the coefficient of friction is decreased to 0.139, resulting in improved wear resistance.

The power supply applies a high voltage or current to the working electrode to form an insulating oxide layer on the metal surface. The high energy provided by the breakdown voltage will break the weaker or more defective parts of the film, and the plasma micro-arc discharge phenomenon will take place [18,19].

Many factors, such as the substrate, electrolyte composition, cathode/anode current density, and duty ratio, affect the thickness, compactness, hardness, abrasion, and corrosion resistance of MAO film [20]. An alkaline electrolyte is relatively more environmentally friendly compared with an acidic solution. So, there is no comprehensive model description for the MAO formation mechanism.

In this study, an MAO film was deposited on aluminum alloy (7075) using different electrical parameters and two electrolyte compositions. The effects of electrolyte composition and electrical parameters on the chemical composition, hardness, abrasion, corrosion, and wear resistance of the MAO film were investigated.

2. Experimental Method and Procedures

2.1. Micro-Arc Oxidation Production

The Huang Chieh Metal Composite Material Tech. Co., Ltd., located in New Taipei City, Taiwan, supplied an aluminum alloy (7075-T6) consisting of Al (90.2%), Zn (5.5%), Mg (2.5%), Cu (1.6%), and other minor components (0.2%). The plate samples sized 30 mm $\times$ 25 mm $\times$ 1.5 mm underwent grinding with abrasive sandpaper of grit size 1000 and ultrasonic cleaning with acetone. An M5 hole was drilled in one corner of the specimen to serve as a holder, and a Teflon gasket was used to prevent any electrolyte leaks during the micro-arc oxidation process due to its high-temperature resistance.

The self-assembled product for micro-arc oxidation (MAO) in this experiment includes an electrolyte tank, stirring and cooling systems, air extraction equipment, power supply, pulse rectifier, and computer control system. A schematic diagram is presented in Figure 1. The electrolyte tank made of 304 stainless steels acted as the counter electrode, while the specimen was the working electrode. The cooling system was set to 11 °C to maintain a constant temperature in the electrolyte tank. Rongxiang Technology Co., Ltd., located in Taichung City, Taiwan, customized the power supply. It can provide up to 600 V-20 A for the positive pole and 300 V-20 A for the negative pole. Two electrolytes ($NaAlO_2$ + NaOH and Na_2SiO_3 + NaOH) were used to produce the micro-arc oxide film. Sodium hydroxide was added as a supporting electrolyte to increase conductivity in the solution. The samples were coated at varying cathode current densities and duty cycles in sodium aluminate and sodium metasilicate systems, and their names are listed in Table 1.
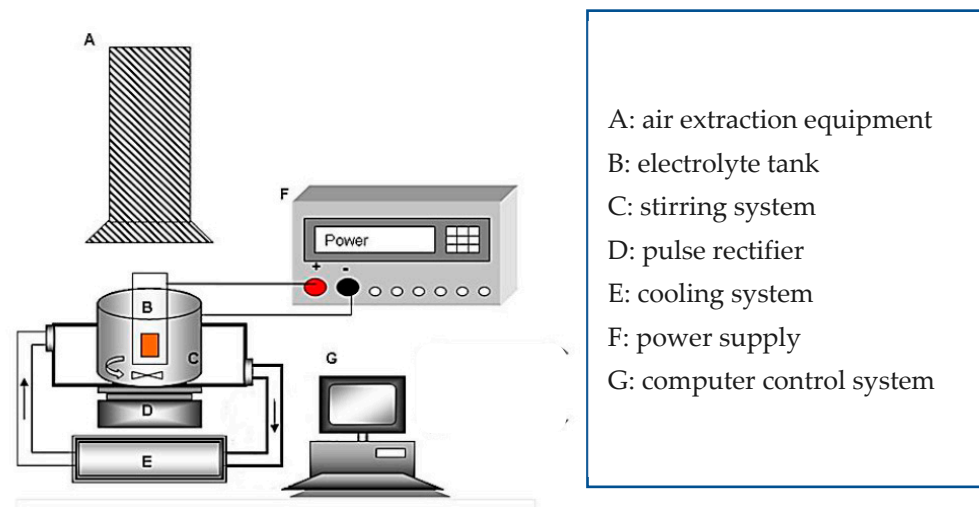
Figure 1. Schematic diagram of micro-arc oxidation system equipment.

Table 1. Experimental parameters and codes of micro-arc oxidation.

Electrolyte Composition	Sodium Aluminate System			Sodium Metasilicate System
Duty Cycle / Cathode Current Density	10%	30%	50%	10%
$-2 \ A/dm^2$	Al-C2-10%	Al-C2-30%	Al-C2-50%	Si-C2-10%
$-6 \ A/dm^2$	Al-C6-10%	Al-C6-30%	Al-C6-50%	Si-C6-10%
$-10 \ A/dm^2$	Al-C10-10%	Al-C10-30%	Al-C10-50%	Si-C10-10%

2.2. Surface Characterization

The microstructure of the micro-arc oxide film with differing electrical parameters and electrolyte composition was analyzed using a scanning electron microscope (JEOL JSM6510, Tokyo, Japan) equipped with an EDS detector. The microscope operated at acceleration voltages ranging from 0.5 kV to 30 kV and magnifications ranging from 5× to 300,000×. The secondary electron image (SEI) mode was primarily used for surface morphology observations, while the backscattered electron image (BEC) mode was used to analyze the micro-arc oxide film's cross-section. Technical term abbreviations are explained when first used. An X-ray diffraction analyzer (Rigaku TTRAX3, Tokyo, Japan) operated with a CuKα light source having a wavelength of 1.5406 Å, a voltage of 50 kV, a current of 300 mA, and diffraction range extending from 20° to 80° at a scan rate of 4°/min was utilized to ascertain the crystalline structure of the film. The diffraction spectrum was then cross-referenced against the diffraction peaks of the JCPDS Card.

Arithmetic mean deviation roughness (Ra) was measured using a Mitutoyo SJ-210 apparatus, manufactured by the Mitutoyo company in the Andover, UK. We measured the hardness of the film with a Vickers hardness machine, specifically, Mitutoyo HM-100, set at an applied load of 0.05 kg and dwell time of 10 s.

2.3. Wear and Corrosion Analysis

A ball-on-disk type abrasion tester, specifically, the CSM TRB 01-05600 nano-tribometer made by CSM Instruments in Peseux, Switzerland, was utilized for both friction and wear analysis. A pair of 6 mm radius grinding balls made of tungsten carbide (WC) were subjected to a load of 7 N for a duration of 800 m, with a 3 mm rotation radius and 15 cm/s rotation speed. The worn surfaces underwent examination with laser scanning confocal microscopy, using the Leica TCS SP5 model produced by Danaher in Washington, DC, USA.

A potentiostat (Multi Autolab/M204, made by Metrohm Company, Herisau, Switzerland) was utilized to investigate the corrosion resistance of the MAO film in a 3.5 wt% NaCl solution (electrolyte) with a contact area of 1.676 cm^2. The system used a saturated calomel electrode (SCE) as the reference electrode, a platinum sheet as the counter electrode, and the specimen as the working electrode. The potentiodynamic polarization curves were taken within the range of −0.2 V to 0.8 V at a scan rate of 1 mV/s. Prior to the measurement, the open circuit potential (OCP) was established for 1 h. Corrosion potential (Ecorr) and corrosion current were obtained by measuring potentiodynamic polarization curves, also known as Tafel curves.

3. Results and Discussion

3.1. Micro-Arc Oxidation Discharge Behavior

There are multiple parameters that can be altered during the micro-arc oxidation (MAO) process. The electrolyte utilized has a significant influence on the resulting MAO film. Figure 2 displays the voltage–time graph of both the 7075 aluminum alloy and the Al-C6-30% specimen with an MAO film. It is evident that the voltage experiences a rapid and linear increase in the initial period, with a large quantity of bubbles emerging on the specimen surface due to the creation of a porous columnar passivation layer during the anodic treatment [15]. The significant changes occurred when the voltage approached point "X" on the curve, and a white spark was observed on the specimen.
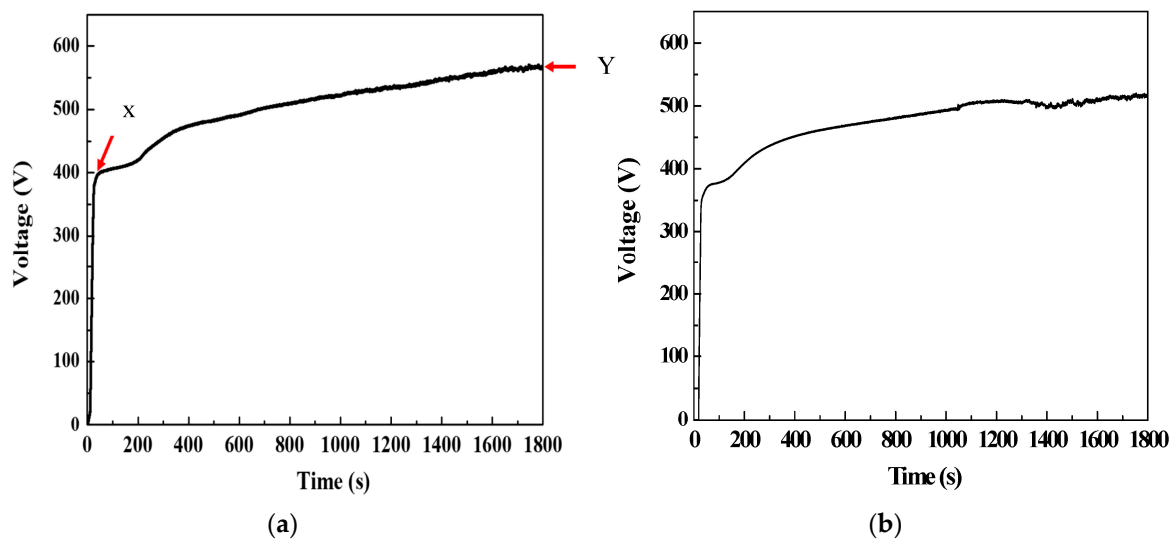

Figure 2. MAO discharge curve of (**a**) aluminum alloy 7075 and (**b**) Al-C6-30%.

The white sparks transform gradually into yellow and orange-red arc points with increasing energy over time [21]. The distribution density of these arc points changes from dense to sparse and gradually larger. The voltage–time plot labels the points "X" and "Y" as spark voltage and final voltage. Table 2 summarizes the final and spark voltage at various duty ratios and cathode current densities.

Table 2. Voltage of MAO at various electrical parameters and electrolytes.

Sample		Sodium Aluminate		Sodium Metasilicate	
Current Density (A/dm^2)	Duty Ratio	Sparking Voltage (V)	Final Voltage (V)	Sparking Voltage (V)	Final Voltage (V)
C2	10%	418.3	556.9	389.8	531.6
C6	10%	418.3	599.3	381.3	545.6
C10	10%	418.1	605	366	542.1
C2	30%	384.4	531.1		
C6	30%	381.5	560.3		
C10	30%	380	565.1		
C2	50%	380.4	520.6		
C6	50%	375.7	549.1		
C10	50%	374.1	544.8		

Increasing the duty cycle leads to a higher ratio of time (τ_{on}^+) that turns on during the discharge cycle, and the passivation film on the aluminum alloy surface is initially thin. When subjected to continuous power-on time with a large duty cycle, the thinner film can break down [22]. Spark discharge occurs when the film is thinner at a low-duty cycle due to sufficient energy to break it down. Therefore, regardless of the magnitude of the applied cathode current, the spark voltage is high when the duty cycle is low [23]. The time between the start of the spark voltage and the final voltage corresponds to the period of growth of the micro-arc oxide film. Assuming constant electrical parameters and electrolyte composition, the final voltage is usually associated with the thickness of the film [24]. It is evident from Table 2 that increasing the duty cycle results in a decrease in both the spark voltage and the final voltage value. From Table 2, it is evident that the spark and final voltages for the sodium meta-silicate system are significantly lower than those for the sodium aluminate system at the same cathodic current density and duty ratio.

The low voltage in the sodium metasilicate system is due to higher conductivity and the film-forming mechanism. Furthermore, the micro-arc discharge behavior, affected by different electrical parameters, can result in varied voltages at distinct cathode current densities. The difference between the Si-rich area and the Al-rich area leads to discharge instability. Efficient dispersion of the anion SiO$_3$ can be achieved with high spatial density discharge under a low-duty cycle. Although the Si-C10-10% discharge becomes unstable in the later stages, the spark voltage remains at 366 V. Adequate energy is necessary to break the film and initiate sparking when the film thickness is greater [25].

3.2. Macroscopic View and Microstructure Analysis of the Film

The surface morphology and microstructure of the micro-arc oxide film are strongly influenced by the plasma discharge behavior. The surface morphology of the film under different electrical parameters in sodium aluminate is shown in Figure 3. Distinct muffin structures and large fluctuations can be observed at low-duty cycles (Figure 3a,d,g). The muffin structure is the channel left by the discharge during the micro-arc oxidation process [26]. It can be seen from Figure 3 that the arc attacks the oxide film at the weaker point, and the film is remelted at the low-duty cycle. The remelted film solidifies to grow up, and the arc is transferred to other weak points [27]. The film grows more uniformly and flatter at relatively high duty ratios with longer discharge times, as shown in Figure 3c,f,i.
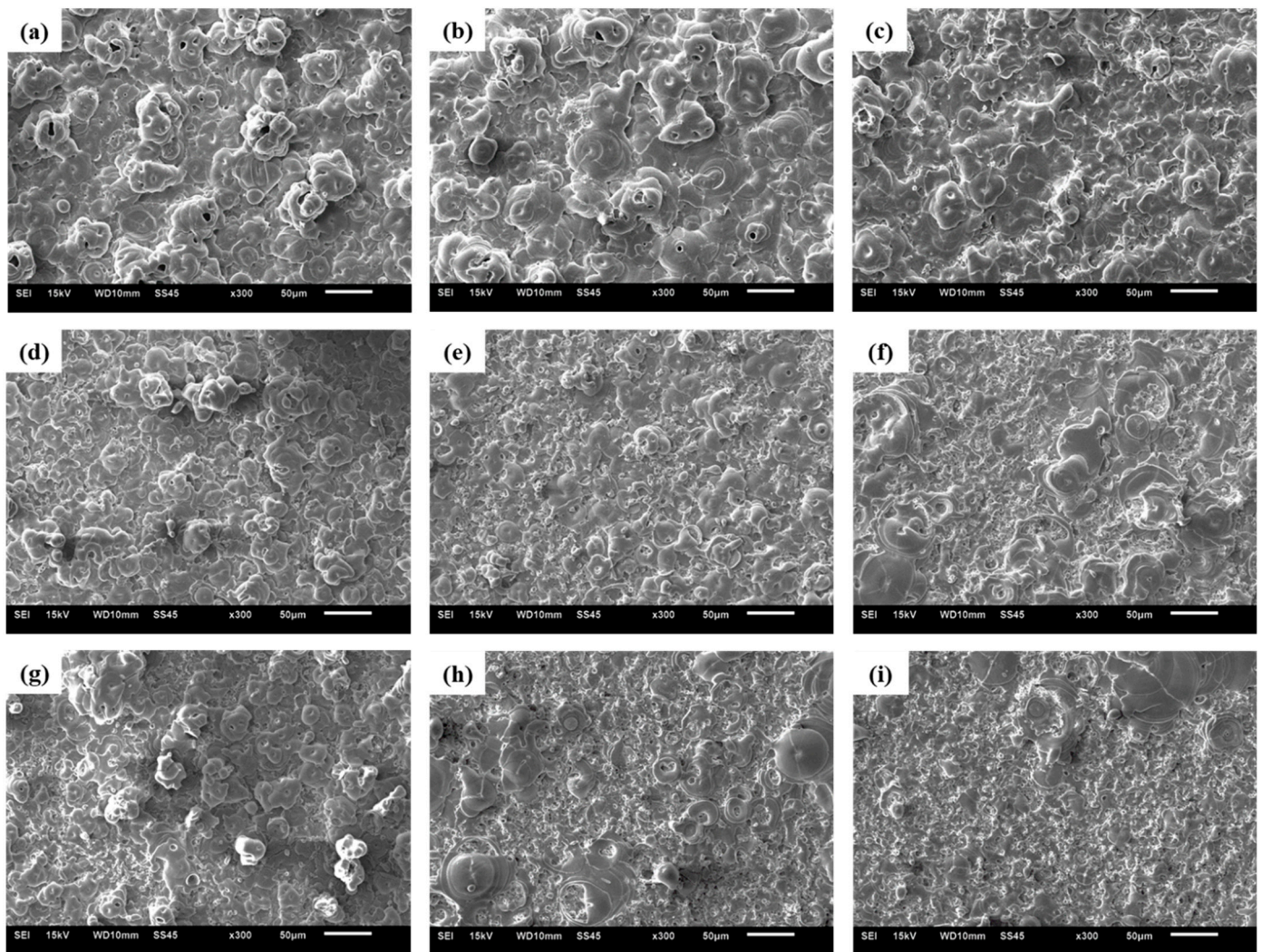
Figure 3. SEM images of the surface morphology of (**a**) Al-C2-10%, (**b**) Al-C2-30%, (**c**) Al-C2-50%, (**d**) Al-C6-10%, (**e**) Al-C6-30%, (**f**) Al-C6-50%, (**g**) Al-C10-10%, (**h**) Al-C10-30%, and (**i**) Al-C10-50%.

It is evident from Figure 3 that as the cathode current increases, the muffin structures decrease gradually, giving way to numerous small holes on the surface. These small pores develop due to the escape of oxygen ions (O^{-2}) to the film's surface under the effect of a strong negative bias electric field. Hence, with the application of a sufficiently large cathodic current, an abundance of dense small pores emerges on the film's surface to replace the muffin structures [15,23].

Different electrolyte components exhibit various performances on the discharge behavior of micro-arc oxidation plasma, resulting in a significant difference in the microstructure of the film. The micro-arc oxidation film of the sodium metasilicate system demonstrates randomly dispersed bubble-like nodular structures, while some conglomerate structures appear (refer to Figure 4). In contrast, the sodium aluminate system forms a smoother muffin-like structure. The region rich in Si due to the Si-Al-O compound forms the nodular structure of these bubbles. The presence or absence of violent arc discharge determines the size of the muffin structure [28,29]. According to Figure 4, an increase in cathode current density results in the formation of a strong muffin structure with noticeable protrusions under the negative electric field.
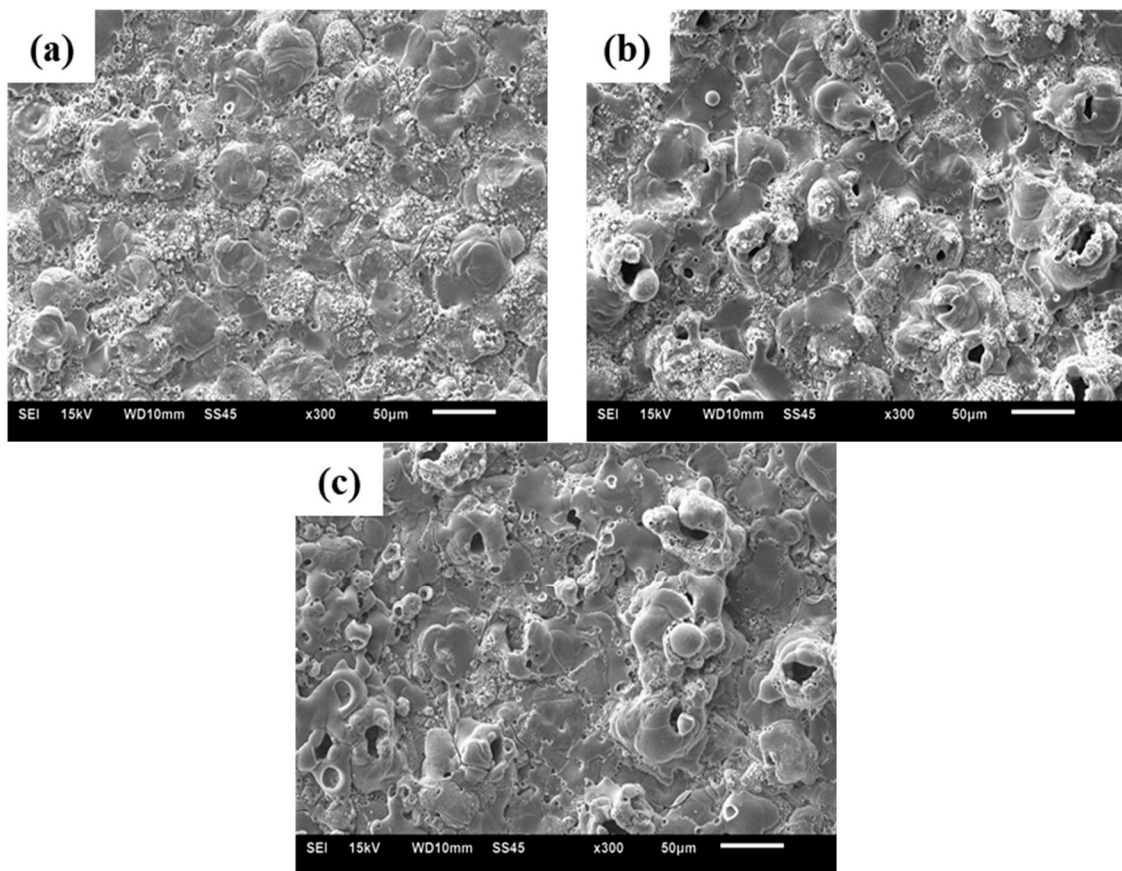
Figure 4. SEM images of surface morphology of (**a**) Si-C2-10%, (**b**) Si-C6-10%, and (**c**) Si-C10-10%.

The cross-sectional structure of the MAO film under various electrical parameters in the sodium aluminate system is shown in Figure 5. The layer exhibits numerous micrometer-sized pores when operating at a 10% duty cycle.

High-pressure oxygen is generated through discharge and erupts from the interior to the surface, which subsequently cools rapidly, resulting in hole formation at the discharge channel edges. Duty cycle increments (see Figure 5b,c) lead to an increase in hole numbers. Contributing to the internal and external growth of the film, duty cycle increments are considered beneficial. The diffusion occurs toward the substrate, where oxygen ions (O^{-2}) react with aluminum ions (Al^{+3}) at a high temperature and pressure, generating alumina that enhances film growth [27]. The surrounding electrolyte components enter the discharge channel and react to form oxides.

It is clear from the cross-sectional images (Figure 6) that increasing in the duty cycle is beneficial to the growth of the film and effectively reduces the pore size in the film. The discharge time is longer at higher duty cycles, and the film grows more uniformly and flatly [30]. The results correspond to the surface morphology in Figure 4. As the cathode current density is increased, the density of the film is obviously improved. These small holes come from the oxygen trapped in the molten oxide, and the size of the pores is not more than 1 micron. However, oxygen has high solubility at high temperatures and pressures and should be dissolved in the molten oxide [23,31]. If the arc duration is short at the low-duty cycle, the undissolved and trapped oxygen will rapidly cool and solidify, leaving holes in the molten oxide.
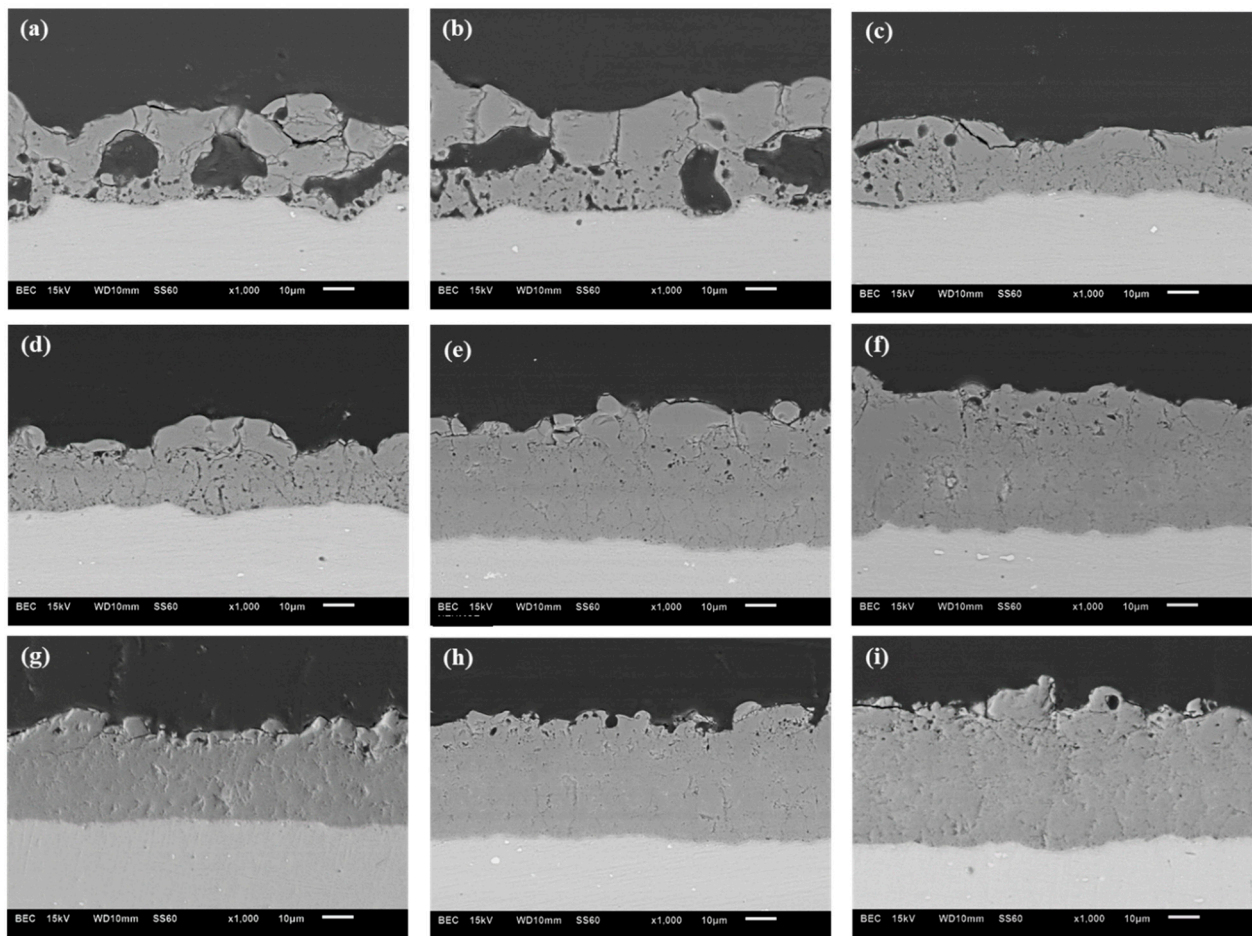
Figure 5. Cross sectional images of MAO films (**a**) Al-C2-10%, (**b**) Al-C2-30%, (**c**) Al-C2-50%, (**d**) Al-C6-10%, (**e**) Al-C6-30%, (**f**) Al-C6-50%, (**g**) Al-C10-10%, (**h**) Al-C10-30%, and (**i**) Al-C10-50%.

Whether in the sodium metasilicate system or sodium aluminate system, holes caused by oxygen become ionized as the negative electric field strength increases. With an increase in cathode current density, the quantity of holes is significantly reduced, thus enhancing the compactness of the film. This trend is akin to that observed in the sodium aluminate system [30,32].

The thickness of each micro-arc oxide film for every electrical parameter is summarized in Table 3. The trends show that Al-C2 consistently has the smallest film thickness, despite duty cycle differences. Al-C2 has more pores, generating a significant amount of oxygen during discharge and drastically reducing current efficiency. As the cathode current density increases, the film thickness increases [31,32]. The film thickness of Al-C2-50% is greater than that of Al-C2-30% in the Al-C2 film when operating at higher duty cycles. The proportion of pores in Al-C2 is larger, leading to a reduced film thickness. Nevertheless, the Al-C6 and Al-C10 layers exhibit a higher density than the Al-C2 film and lack significant pores. When the duty cycle is relatively high (30%, 50%), the discharge time is prolonged, enabling the film layer to grow for an extended period. Consequently, the thickness of the film layer surpasses that of the 10% duty cycle.
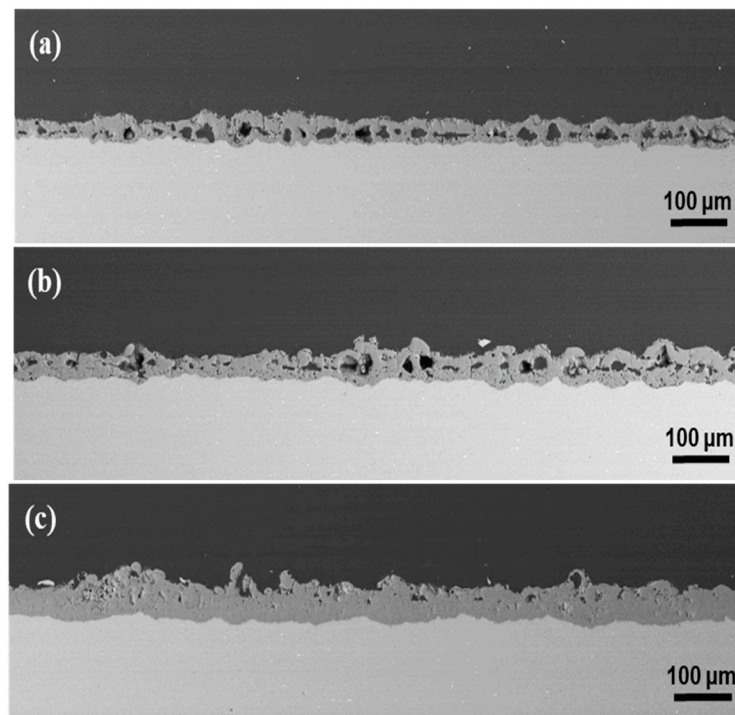
Figure 6. Cross sectional images of (**a**) Si-C2-10%, (**b**) Si-C6-10%, and (**c**) Si-C10-10%.

Table 3. Thickness (μm) of the MAO film for each electrical parameter.

Cathode Current Density (A/dm^2) / Duty Ratio	Sodium Aluminate			Sodium Metasilicate
	10%	30%	50%	10%
C2	26.28	26.64	30.84	30.46
C6	30.72	40.31	42.76	37.94
C10	34.05	40.69	41.65	48.43

Similarly, the thickness of the micro-arc oxide film increases with an increase in the cathode current density in the sodium metasilicate system. Additionally, the film thickness in the sodium metasilicate system is greater under the same electrical parameters. The low initial arcing voltage could be due to the passivation film created by sodium metasilicate having a low dielectric resistance or faster reactivity. This results in a higher film formation rate for the sodium metasilicate system under the same output current [33].

From the results recorded in Table 4, it is evident that the surface roughness decreases with an increase in the duty cycle and cathode current density. Notably, the Al-C6-10% film and Si-C6-10% exhibit the highest surface roughness. The proportion of pores present in the surface correlates directly with the surface roughness.

Table 4. The surface roughness Ra (μm) of the MAO film for each electrical parameter.

Cathode Current Density (A/dm^2) / Duty Ratio	Sodium Aluminate			Sodium Metasilicate
	10%	30%	50%	10%
C2	4.37	3.92	3.01	3.35
C6	6.03	3.64	2.83	6.43
C10	3.57	2.48	2.12	5.51

The micro-arc oxidation process mainly affects the surface roughness [34]. A large cathodic current density can assist in moving oxygen toward the electrolyte in the pores. If the oxygen can fully escape the film surface, the pores vanish in the film, which promotes

surface melting [35]. The flow of oxide enhances the uniformity of the film and decreases the surface roughness. If oxygen is unable to escape entirely from the film layer's surface and only flows from the substrate's interior to the outside, then pores continue to exist within the film layer, resulting in increased surface roughness. Table 4 indicates that the surface roughness rises and then decreases as the cathode current density increases. The oxygen does not detach from the surface in Si-C6-10%, resulting in a greater surface roughness as compared with Si-C2-10%. Although the surface roughness of Si-C10-10% decreased, it is still higher than that of Si-C2-10%, indicating that some oxygen in the pores escapes to the electrolyte, while some remains near the surface.

3.3. Analysis of Composition and Structure

An X-ray diffraction (XRD) analysis of micro-arc oxide films was conducted under all electrical parameters and both electrolyte systems, as shown in Figure 7. The micro-arc oxide film in the sodium aluminate system is found to consist of α-Al_2O_3 and γ-Al_2O_3 crystalline phases. The strength of these phases is primarily influenced by the holes and thickness of the film. The denser and thicker the film, the stronger the alumina crystal phase becomes [29,36]. The aluminum ions (Al^{+3}) from the substrate react with hydroxide ions (OH^-) from the electrolyte to produce γ-Al_2O_3 at low temperatures and α-Al_2O_3 at high temperatures.
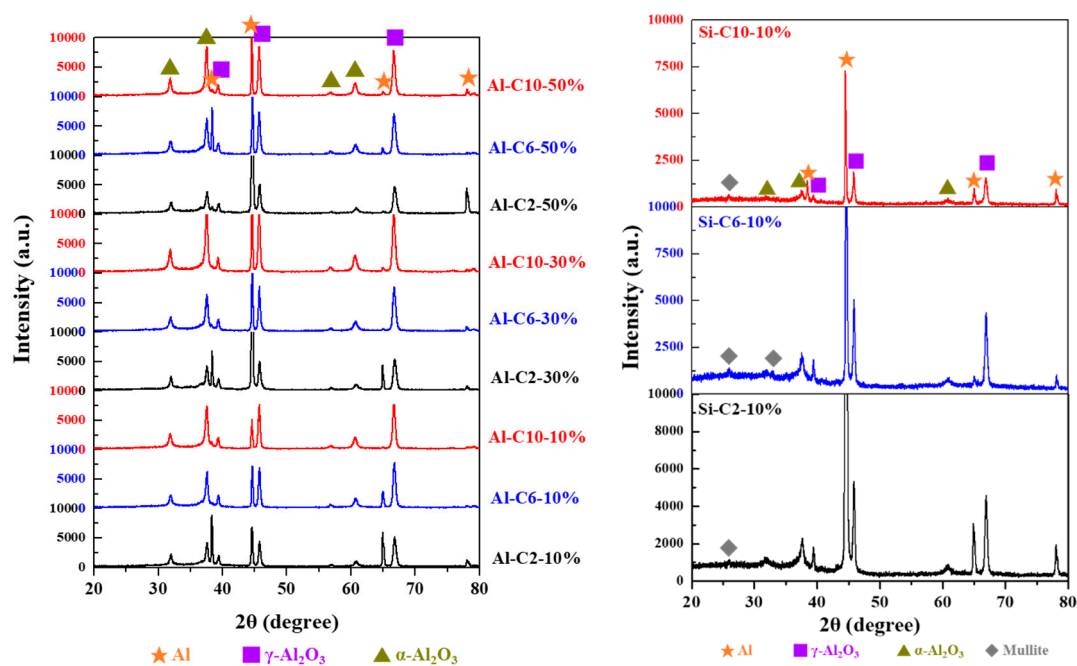

Figure 7. XRD analysis of the micro-arc oxide film for each electrical parameter in the sodium aluminate system.

The composition of the film in the sodium metasilicate system predominantly consists of γ-Al_2O_3 with a minor quantity of α-Al_2O_3 and mullite ($Al_6Si_2O_{13}$) crystal phase. The robust Al phase detected in the Si-C2-10% film is primarily due to its thin film thickness and hole existence. In contrast, the mullite phase mainly emerges at the diffraction angles of 26°, 33°, and 35°, among others, which may be due to its negligible concentration or an insignificant peak in the non-crystalline state. Furthermore, upon comparison with the sodium aluminate system, it is evident that the low-angle region of the sodium metasilicate system exhibits broad and truncated peaks, suggesting the presence of the amorphous state in a certain portion of the system [33,37,38].

Table 5 presents the micro-hardness outcomes of the micro-arc oxidation film with various electrical parameters in the sodium aluminate and sodium metasilicate systems. In

the Al-C2-10% and Si-C2-10% films, the pores are excessively large to cover the film area entirely, and the hardness indentation test cannot display the hardness value. The hardness of the film amounted to 860 HV for Al-C2-50%, which is due to its higher compactness. If the porosity is high, then the depth and size of the indentation will deepen, resulting in a lower hardness. The sodium metasilicate system mainly comprises γ-Al_2O_3 along with a small quantity of α-Al_2O_3 and mullite, consisting of amorphous material. The hardness of γ-Al_2O_3 is relatively lower than that of α-Al_2O_3. Consequently, the dense film's hardness in the sodium metasilicate system is inherently lower, thereby directly affecting the film's wear resistance.

Table 5. Microhardness (HV) of the MAO film for each electrical parameter.

Cathode Current Density (A/dm^2) / Duty Ratio	Sodium Aluminate			Sodium Metasilicate
	10%	30%	50%	10%
C2	---	823	860	---
C6	1364	1310	1396	621
C10	1374	1306	1504	1049

3.4. Analysis of Wear Properties

The wear resistance of the micro-arc oxidation film is influenced by its compactness, thickness, and hardness. The coefficient of friction during the abrasion test is affected by factors like the surface roughness and hardness of the film [39]. Figure 8 illustrates the coefficient of friction curves at different electrical parameters in the substrate and electrolyte system. Repetitive wear of the grinding balls and film causes abrasion wear, and the surface roughness is directly associated with it. The coefficient of friction (COF) is mainly dependent on the substrate and film structure. Figure 8 demonstrates that coefficient of friction for different electrolytes under different electrical parameters. It can be observed that increase in cathode current density leads to increase in coefficient of friction. Films with more pores exhibit a lower friction coefficient.

The friction curve's sudden increase or decrease in friction coefficient indicates significant changes in the film layer during abrasion, such as changes to material properties. For instance, curve 8b displays a sudden decrease in the coefficient at 800m, and curve 8h exhibits a sudden increase in the friction coefficient. These changes suggest that the grinding ball ground down to the substrate.

An analysis of Figure 9 shows a sudden drop in the friction coefficient of the Si-C2-10% film to around 0.4 after sliding for approximately 150 meters. The same results are observed for the substrate, indicating that the grinding ball is ground from the film layer to the aluminum alloy substrate. The Si-C2-10% film has numerous holes, which results in poor wear resistance, and the friction coefficient gradually increases until it reaches a stable value. As the number of turns increases, the contact area expands since the grinding ball does not have complete contact with the undulating film initially [40]. The friction coefficient of the Si-C6-10% abrasive layer is approximately 0.5, while that of the Si-C10-10% film is about 0.6. The Si-C10-10% film layer is denser, as seen in Table 3, resulting in more contact area between the film layer and the grinding ball during the wear process. As a result, the friction coefficient of Si-C10-10% is greater than that of Si-C6-10%.
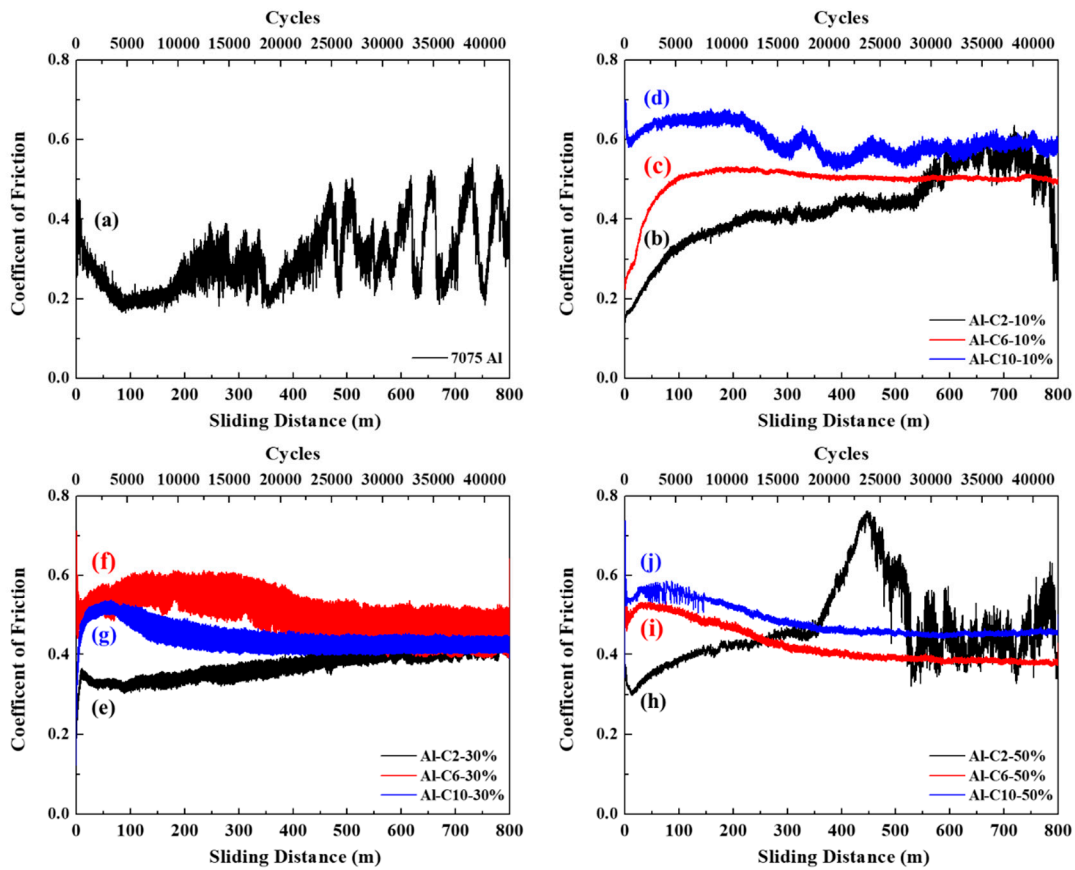
Figure 8. Friction coefficient–sliding distance diagram for (**a**) 7075 aluminum alloy, (**b**) Al-C2-10%, (**c**) Al-C6-10%, (**d**) Al-C10-10%, (**e**) Al-C2-30%, (**f**) Al-C6-30%, (**g**) Al-C10-30%, (**h**) Al-C2-50%, (**i**) Al-C6-50%, and (**j**) Al-C10-50%.
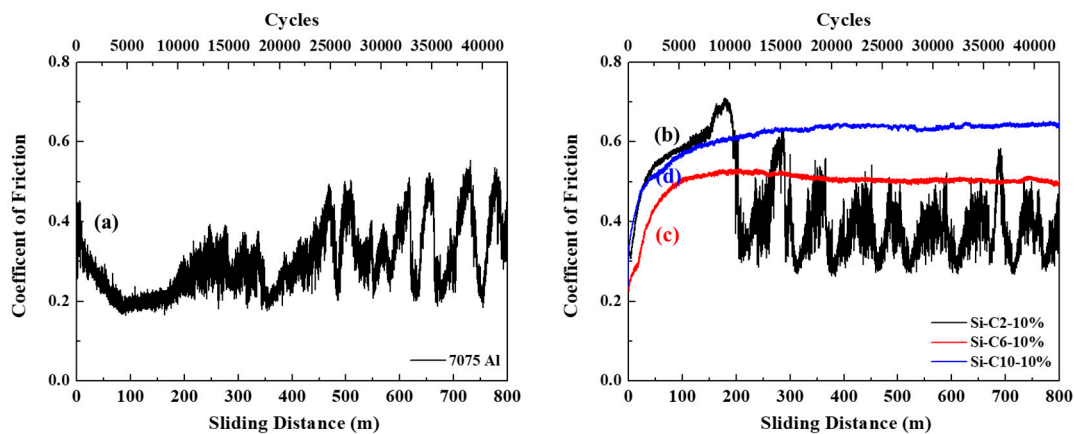

Figure 9. Friction coefficient–sliding distance diagram for (**a**) 7075 aluminum alloy, (**b**) Si-C2-10%, (**c**) Si-C6-10%, and (**d**) Si-C10-10%.

The morphology of the wear track for the MAO film in the sodium aluminate system and the degree of depression are illustrated in Figure 10. A summary of the wear depth and width is provided in Tables 6 and 7. The findings in Figure 10 and Tables 6 and 7 demonstrate that with an increase in cathode current density or duty cycle, the wear track's width and depth tend to become narrower and shallower. Wear resistance is closely linked to film compactness, and the Al-C10-50% film exhibits the highest level of compactness and wear resistance. This finding is consistent with the study conducted by Konstantin et al. [41], which demonstrates that film compactness is proportional to current frequency.

Wear resistance is closely linked to film compactness, and the Al-C10-50% film exhibits the highest level of compactness and wear resistance. Furthermore, greater compactness results in better corrosion and wear resistance.
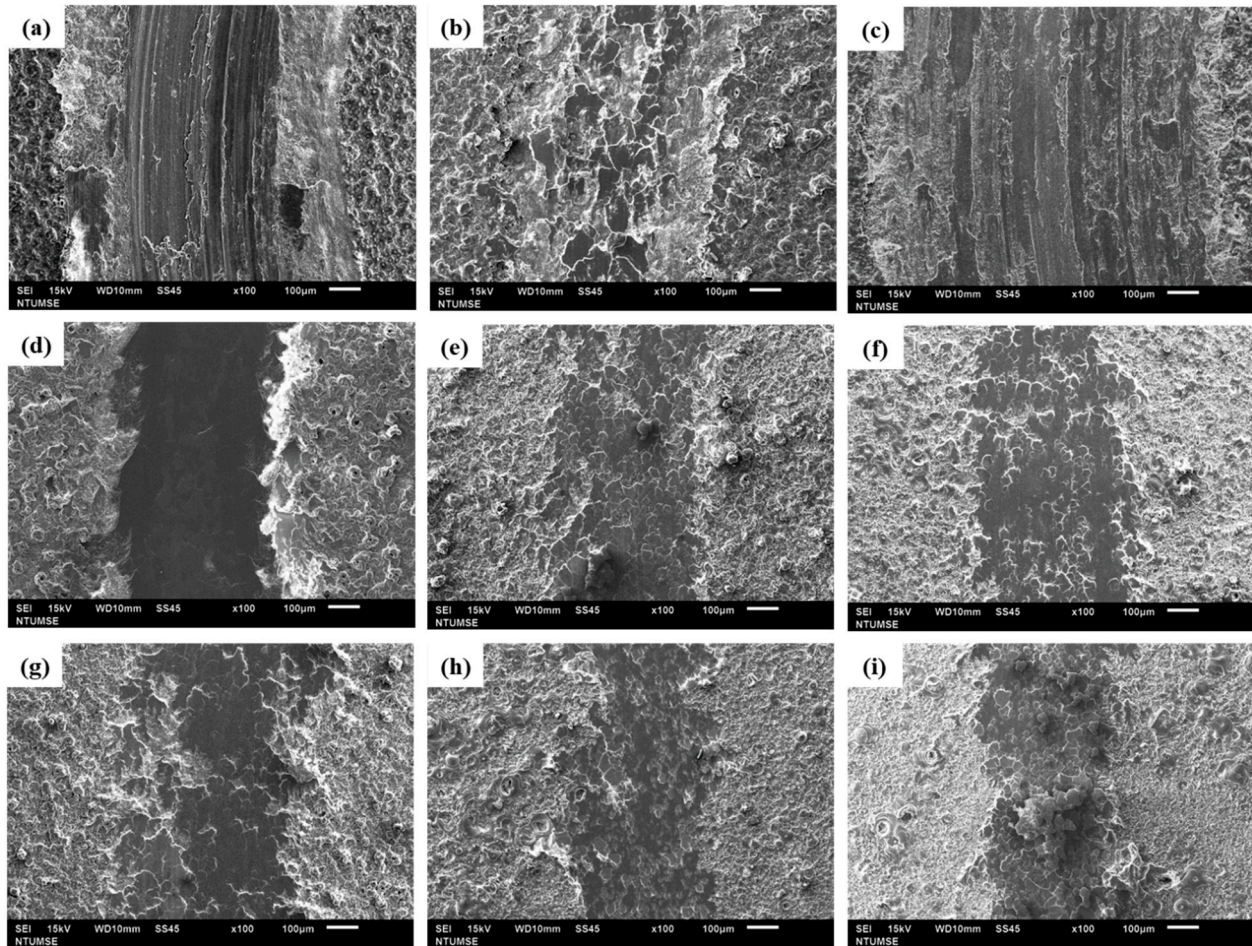

Figure 10. Wear track of the MAO film: (**a**) Al-C2-10%, (**b**) Al-C2-30%, (**c**) Al-C2-50%, (**d**) Al-C6-10%. (**e**) Al-C6-30%, (**f**) Al-C6-50%, (**g**) Al-C10-10%, (**h**) Al-C10-30%, and (**i**) Al-C10-50%.

Table 6. Abrasion track width (μm) of the MAO film for each electrical parameter.

Duty Ratio Cathode Current Density (A/dm^2)	Sodium Aluminate			Sodium Metasilicate
	10%	**30%**	**50%**	**10%**
C2	993.90	665.38	1021.13	1529.50
C6	715.62	465.48	435.83	901.83
C10	601.21	397.24	394.62	842.67

Table 7. Depth (μm) of abrasion trajectory of the MAO film for each electrical parameter.

Duty Ratio Cathode Current Density (A/dm^2)	Sodium Aluminate			Sodium Metasilicate
	10%	**30%**	**50%**	**10%**
C2	54.03	43.63	20.05	111.97
C6	16.17	7.08	4.45	29.76
C10	9.63	3.72	3.57	23.77

The Al-C2-10% and Al-C2-50% films are ground to the substrate, and the depth and width of the abrasion are not only affected by the micro-arc oxidation film but also include

the abrasion of the substrate. The Al-C2-10% film, which has a thickness of 26.28 μm, exhibits significant porosity and the poorest wear resistance compared with all other parameters.

The surface morphology of worn film within the sodium metasilicate system is illustrated in Figure 11. The findings indicate that the Si-C2-10% film wear track depth is approximately 112 μm. Furthermore, the Si-C10-10% film is denser and has minimal perforations. Its width is narrow, the depth shallow, and the wear resistance is optimal [42]. The width and depth of the abrasion track for the film utilizing the sodium metasilicate and sodium aluminate systems are compared in Tables 6 and 7. The abrasion resistance is ranked as follows: Al-C10-50% > Al-C10-30% > Al-C6-50% > Al-C6-30% > Al-C10-10% > Al-C6-10% > Al-C2-30% > Si-C10-10% > Si-C6-10% > Al-C2-50% > Al-C2-10% > Si-C2-10%. The wear resistance of the aforementioned micro-arc oxide film is primarily influenced by the film's hardness, thickness, compactness, and composition [9].
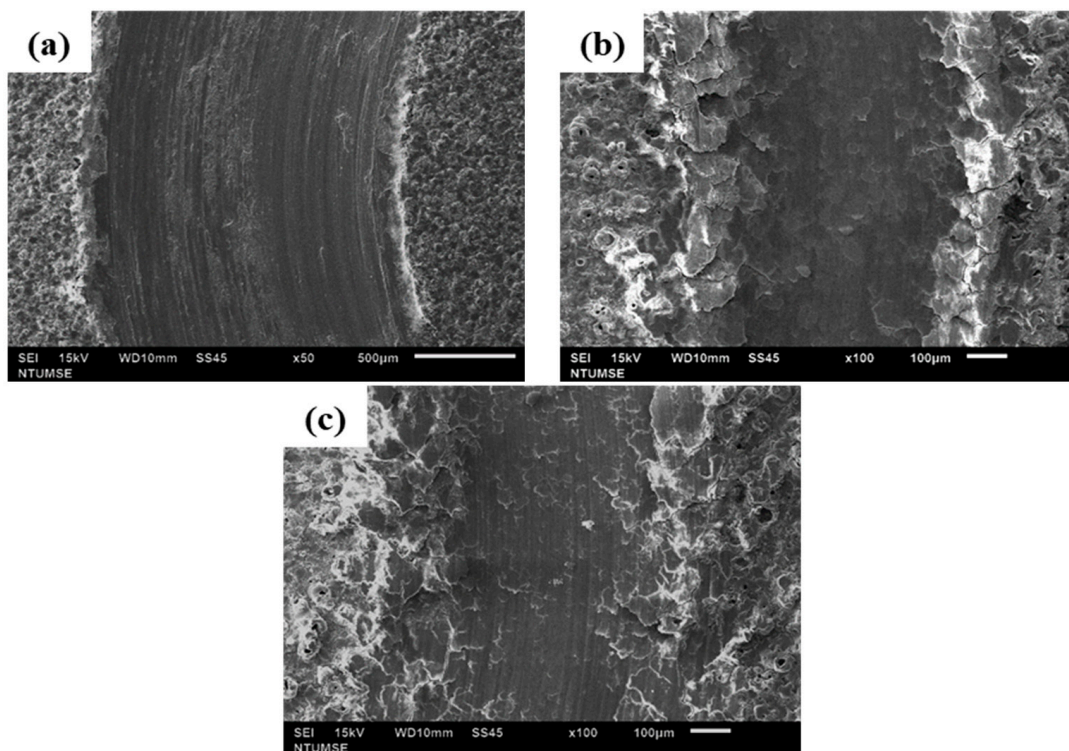

Figure 11. Wear track of the MAO film: (**a**) Si-C2-10%, (**b**) Si-C6-10%, and (**c**) Si-C10-10%.

Based on the aforementioned order, it is evident that, apart from the thinner films of Al-C2-30% and Al-C2-10%, the sodium aluminate system displays better resistance to abrasion than the sodium metasilicate system [37].

3.5. Analysis of Corrosion Properties

Polarization curves of the MAO film under the sodium aluminate system are shown in Figure 12. The cathodic polarization zone curve displays periodic oscillations, which signify the onset of pitting corrosion of aluminum alloy in NaCl solution. The hydrogen evolution reaction becomes more intense, leading to an increase in the cathode current value [39,43]. The aluminum alloy forms a passivation film to protect the substrate from hindering the hydrogen evolution reaction. The current density of corrosion decreases, implying excellent adherence to the substrate [6,44]. The overall area is small, and the corrosion resistance is optimal. The identical phenomenon can be witnessed in the polarization curves with duty ratios of 30% and 50%. Tables 8 and 9 summarize the corrosion potential

and corrosion current density of polarization curves. It can be observed that corrosion potential is enhanced with the rise in cathode current.
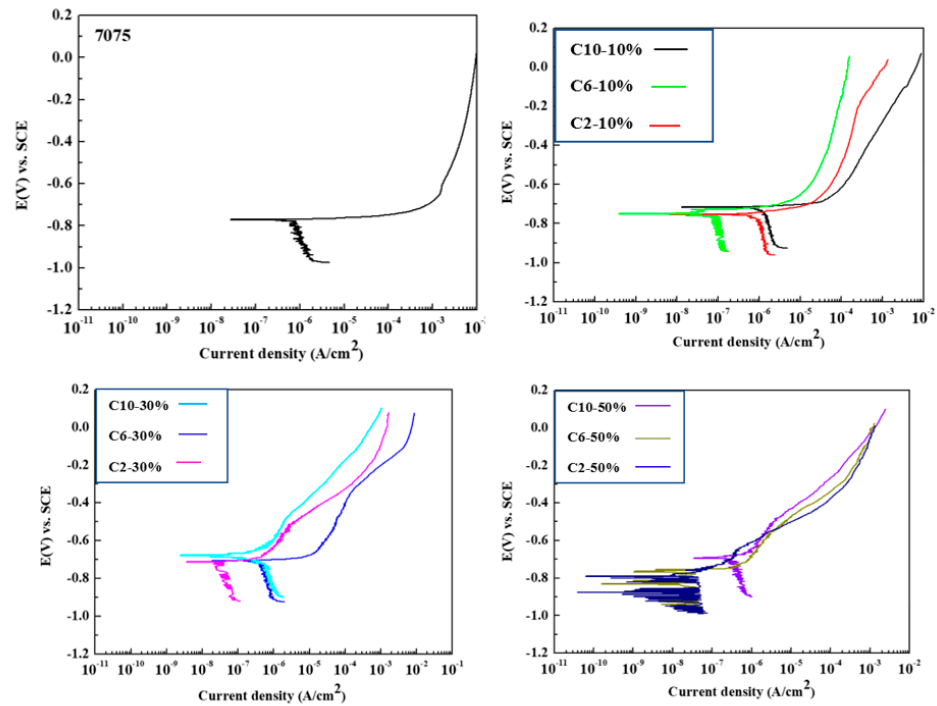

Figure 12. Potential polarization curve of the MAO film for each electrical parameter in the sodium aluminate system.

Table 8. E_{corr} (V_{SCE}) of the polarization curve of MAO film for each electrical parameter.

Cathode Current Density (A/dm²)	Duty Ratio	Sodium Aluminate			Sodium Metasilicate
		10%	30%	50%	10%
C2		−0.877	−0.753	−0.712	−0.771
C6		−0.832	−0.750	−0.705	−0.736
C10		−0.716	−0.695	−0.677	−0.720

Table 9. I_{corr} (A/cm²) obtained from the polarization curve of the MAO film for each electrical parameter.

Cathode Current Density (A/dm²)	Duty Ratio	Sodium Aluminate			Sodium Metasilicate
		10%	30%	50%	10%
C2		4.53×10^{-7}	2.43×10^{-7}	2.16×10^{-7}	1.44×10^{-7}
C6		3.82×10^{-7}	1.85×10^{-7}	1.50×10^{-8}	1.16×10^{-8}
C10		2.57×10^{-7}	1.26×10^{-7}	1.23×10^{-8}	1.20×10^{-8}

Due to the increased film thickness and reduced number of defects, the film demonstrates passivation behavior in the anode area due to its greater resistance to corrosion. In particular, the Ecorr and Icorr of 7075 substrates are −0.777 VSCE and 1.44×10^{-6} A/cm², respectively. It can be deduced from Table 9 that an increase in cathode current density and the duty cycle results in a decrease in corrosion current value, indicating an enhancement in the film's corrosion resistance [41,45]. A greater current density leads to the formation of a more condensed film, thereby ameliorating its corrosion resistance. When comparing the corrosion resistance based on the size of the corrosion current, the results indicate that Al-C10-50% > Al-C6-50% > Al-C10-30% > Al-C6-30% > Al-C2-50% > Al-C2-30% > Al-C10-10% > Al-C6-10% > Al-C2-10%. Additionally, Figure 13 demonstrates that the

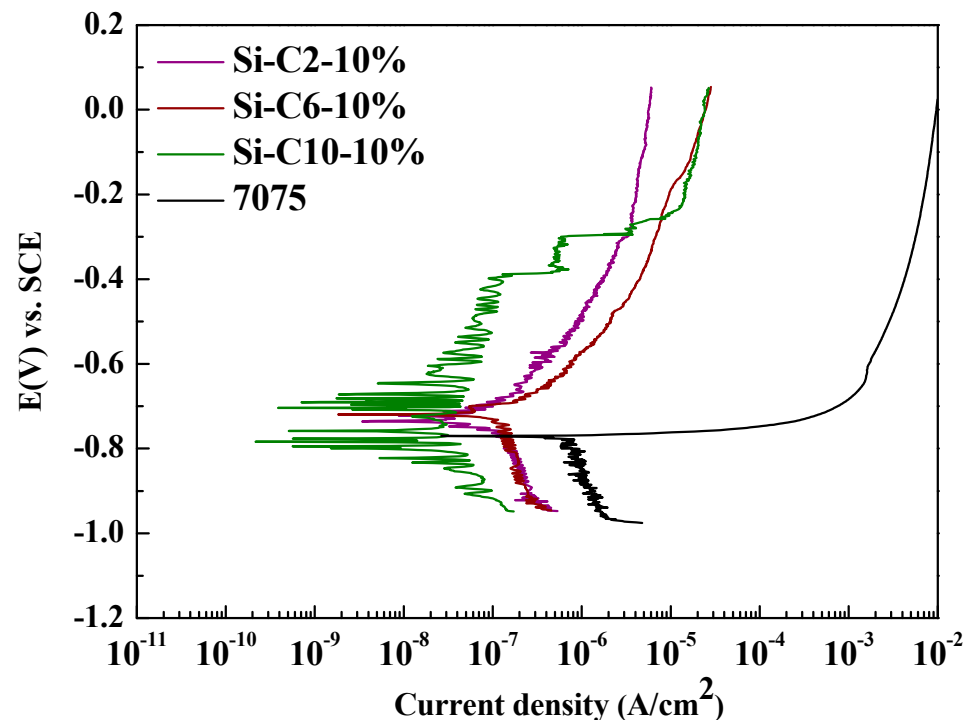Si-C10-10% film possesses the best corrosion resistance within the sodium metasilicates system.

Figure 13. Potential polarization curve of the MAO film for each electrical parameter in the sodium metasilicate system.

4. Conclusions

1. Muffin-shaped structures are smoothly formed on the surface in the sodium aluminate system, whereas nodular structures are developed in the sodium metasilicate system.
2. The MAO film formed in the sodium aluminate system mainly consist of α-Al_2O_3 and γ-Al_2O_3, and the film of the sodium metasilicate system mainly consists of γ-Al_2O_3 with a small amount of α-Al_2O_3 and mullite amorphous phases.
3. The MAO film formed in the sodium aluminate system film exhibits a maximum hardness of 1300–1500 HV, whereas that formed in the metasilicate system is 1049 HV.
4. The MAO film formed in the sodium aluminate system exhibits better wear resistance in comparison with the sodium metasilicate system, irrespective of density. However, the films formed in the sodium metasilicate system demonstrate improved corrosion resistance in the NaCl solution.

Author Contributions: Conceptualization, H.-C.L.; methodology, T.-Y.W.; formal analysis, T.-Y.W.; investigation, T.-Y.W.; resources, H.-C.L.; data curation, T.-Y.W.; writing—original draft preparation, A.A.; supervision, H.-C.L.; project administration, H.-C.L.; funding acquisition, H.-C.L. All authors have read and agreed to the published version of the manuscript.

Data Availability Statement: The data presented in this study are available on request from the corresponding author.

Conflicts of Interest: Authors have no conflict of interest.

References

1. Dursun, T.; Soutis, C. Recent developments in advanced aircraft aluminium alloys. *Mater. Des.* **2014**, *56*, 862–871. [CrossRef]
2. Heinz, A.; Haszler, A.; Keidel, C.; Moldenhauer, S.; Benedictus, R.; Miller, W.S. Recent development in aluminium alloys for aerospace applications. *Mater. Sci. Eng. A* **2000**, *280*, 102–107. [CrossRef]
3. Birbilis, N.; Buchheit, R.G. Electrochemical Characteristics of Intermetallic Phases in Aluminum Alloys. *J. Electrochem. Soc.* **2005**, *152*, B140. [CrossRef]
4. Villuendas, A.; Jorba, J.; Roca, A. The Role of Precipitates in the Behavior of Young's Modulus in Aluminum Alloys. *Metall. Mater. Trans. A* **2014**, *45*, 3857–3865. [CrossRef]
5. Jain, S.; Lim, M.L.C.; Hudson, J.L.; Scully, J.R. Spreading of intergranular corrosion on the surface of sensitized Al-4.4Mg alloys: A general finding. *Corros. Sci.* **2012**, *59*, 136–147. [CrossRef]
6. Birbilis, N.; Cavanaugh, M.K.; Buchheit, R.G. Electrochemical behavior and localized corrosion associated with Al_7Cu_2Fe particles in aluminum alloy 7075-T651. *Corros. Sci.* **2006**, *48*, 4202–4215. [CrossRef]
7. Malayoglu, U.; Tekin, K.C.; Malayoglu, U.; Shrestha, S. An investigation into the mechanical and tribological properties of plasma electrolytic oxidation and hard-anodized coatings on 6082 aluminum alloy. *Mater. Sci. Eng. A* **2011**, *528*, 7451–7460. [CrossRef]
8. Krishna, L.R.; Purnima, A.S.; Sundararajan, G. A comparative study of tribological behavior of microarc oxidation and hard-anodized coatings. *Wear* **2006**, *261*, 1095–1101. [CrossRef]
9. Shao, L.; Li, H.; Jiang, B.; Liu, C.; Gu, X.; Chen, D. A Comparative Study of Corrosion Behavior of Hard Anodized and Micro-Arc Oxidation Coatings on 7050 Aluminum Alloy. *Metals* **2018**, *8*, 165. [CrossRef]
10. Yerokhin, A.L.; Snizhko, L.O.; Gurevina, N.L.; Leyland, A.; Pilkington, A.; Matthews, A. Discharge characterization in plasma electrolytic oxidation of aluminium. *J. Phys. D Appl. Phys.* **2003**, *36*, 2110–2120. [CrossRef]
11. Matykina, E.; Berkani, A.; Skeldon, P.; Thompson, G.E. Real-time imaging of coating growth during plasma electrolytic oxidation of titanium. *Electrochim. Acta* **2007**, *53*, 1987–1994. [CrossRef]
12. Liu, X.; Zhu, L.; Liu, H.; Li, W. Investigation of MAO coating growth mechanism on aluminum alloy by two-step oxidation method. *Appl. Surf. Sci.* **2014**, *293*, 12–17. [CrossRef]
13. Sundararajan, G.; Rama Krishna, L. Mechanisms underlying the formation of thick alumina coatings through the MAO coating technology. *Surf. Coat. Technol.* **2003**, *167*, 269–277. [CrossRef]
14. Chen, G.-Y.; Wu, H.-H.; Li, Y.; Chang, H.; Tang, Y.-G. Effect of electrical parameters on characteristics of microarc oxidation coatings of commercially pure titanium in colloid. *Acta Phys. Sin.* **2010**, *59*, 1958. [CrossRef]
15. Wang, J.-H.; Du, M.-H.; Han, F.-Z.; Yang, J. Effects of the ratio of anodic and cathodic currents on the characteristics of micro-arc oxidation ceramic coatings on Al alloys. *Appl. Surf. Sci.* **2014**, *292*, 658–664. [CrossRef]
16. Li, F.; An, M.; Liu, G.; Duan, D. Effects of sulfidation of passive film in the presence of SRB on the pitting corrosion behaviors of stainless steels. *Mater. Chem. Phys.* **2009**, *113*, 971–976. [CrossRef]
17. Chen, J.; Bai, Z.; Xu, J.; Li, W.; Jia, E.; Wang, J. Preparation and tribological properties of MAO-PVA/PTFE self-lubricating composite coating on aluminum alloy surface. *J. Coat. Technol. Res.* 2023. [CrossRef]
18. Mécuson, F.; Czerwiec, T.; Belmonte, T.; Dujardin, L.; Viola, A.; Henrion, G. Diagnostics of an electrolytic microarc process for aluminium alloy oxidation. *Surf. Coat. Technol.* **2005**, *200*, 804–808. [CrossRef]
19. Dunleavy, C.S.; Golosnoy, I.O.; Curran, J.A.; Clyne, T.W. Characterisation of discharge events during plasma electrolytic oxidation. *Surf. Coat. Technol.* **2009**, *203*, 3410–3419. [CrossRef]
20. Hussein, R.O.; Nie, X.; Northwood, D.O. Influence of process parameters on electrolytic plasma discharging behaviour and aluminum oxide coating microstructure. *Surf. Coat. Technol.* **2010**, *205*, 1659–1667. [CrossRef]
21. Tsai, D.-S.; Chou, C.-C. Review of the Soft Sparking Issues in Plasma Electrolytic Oxidation. *Metals* **2018**, *8*, 105. [CrossRef]
22. Terleeva, O.P.; Oh, Y.; Slonova, A.I.; Kireenko, I.B.; Ok, M.-R.; Ha, H.-P. Quantitative Parameters and Definition of Stages of Anodic-Cathodic Microplasma Processes on Aluminum Alloys. *Mater. Trans.* **2005**, *46*, 2077–2082. [CrossRef]
23. Gębarowski, W.; Pietrzyk, S. Growth Characteristics of the Oxide Layer on Aluminium in the Process of Plasma Electrolytic Oxidation. *Arch. Metall. Mater.* **2014**, *59*, 407–411. [CrossRef]
24. Rogov, A.B.; Shayapov, V.R. The role of cathodic current in PEO of aluminum: Influence of cationic electrolyte composition on the transient current-voltage curves and the discharges optical emission spectra. *Appl. Surf. Sci.* **2017**, *394*, 323–332. [CrossRef]
25. Rogov, A.B.; Yerokhin, A.; Matthews, A. The role of cathodic current in plasma electrolytic oxidation of aluminium: Current density 'scanning waves' on complex-shape substrates. *J. Phys. D Appl. Phys.* **2018**, *51*, 405303. [CrossRef]
26. Clyne, T.W.; Troughton, S.C. A review of recent work on discharge characteristics during plasma electrolytic oxidation of various metals. *Int. Mater. Rev.* **2019**, *64*, 127–162. [CrossRef]
27. Xue, W.; Deng, Z.; Chen, R.; Zhang, T. Growth regularity of ceramic coatings formed by microarc oxidation on Al–Cu–Mg alloy. *Thin Solid Film.* **2000**, *372*, 114–117. [CrossRef]
28. Aliasghari, S.; Skeldon, P.; Thompson, G.E. Plasma electrolytic oxidation of titanium in a phosphate/silicate electrolyte and tribological performance of the coatings. *Appl. Surf. Sci.* **2014**, *316*, 463–476. [CrossRef]
29. Sun, X.; Jiang, Z.; Xin, S.; Yao, Z. Composition and mechanical properties of hard ceramic coating containing α-Al2O3 produced by microarc oxidation on Ti–6Al–4V alloy. *Thin Solid Films* **2005**, *471*, 194–199. [CrossRef]
30. Wang, Z.X.; Zhang, J.W.; Ye, F.; Lv, W.G.; Lu, S.; Sun, L.; Jiang, X.Z. Properties of Micro-Arc Oxidation Coating Fabricated on Magnesium under Two Steps Current-Decreasing Mode. *Front. Mater.* **2020**, *7*, 261. [CrossRef]

31. Shu, Y.F.; Jiang, B.; Wang, C.; Song, R.G. Effects of voltage on microstructure and properties of micro-arc oxidation ceramic coatings on AZ31B magnesium alloy under constant current–constant voltage operation mode. *Anti-Corros. Methods Mater.* 2023. [CrossRef]

32. Yao, J.; Wang, S.; Zhou, Y.; Dong, H. Effects of the Power Supply Mode and Loading Parameters on the Characteristics of Micro-Arc Oxidation Coatings on Magnesium Alloy. *Metals* **2020**, *10*, 1452. [CrossRef]

33. Hussein, R.O.; Nie, X.; Northwood, D.O. An investigation of ceramic coating growth mechanisms in plasma electrolytic oxidation (PEO) processing. *Electrochim. Acta* **2013**, *112*, 111–119. [CrossRef]

34. Xu, F.; Luo, L.; Xiong, L.; Liu, Y. Microstructure and corrosion behavior of ALD Al2O3 film on AZ31 magnesium alloy with different surface roughness. *J. Magnes. Alloys* **2020**, *8*, 480–492. [CrossRef]

35. Clavería, I.; Lostalé, A.; Fernández, Á.; Castell, P.; Elduque, D.; Mendoza, G.; Zubizarreta, C. Enhancement of Tribological Behavior of Rolling Bearings by Applying a Multilayer ZrN/ZrCN Coating. *Coatings* **2019**, *9*, 434. [CrossRef]

36. Islamov, D.R.; Gritsenko, V.A.; Lebedev, M.S. Determination of trap density in hafnia films produced by two atomic layer deposition techniques. *Microelectron. Eng.* **2017**, *178*, 104–107. [CrossRef]

37. Balagna, C.; Spriano, S.; Faga, M.G. Characterization of Co-Cr-Mo alloys after a thermal treatment for high wear resistance. *Mater. Sci. Eng. C* **2012**, *32*, 1868–1877. [CrossRef]

38. Li, J.; Cai, H.; Xue, X.; Jiang, B. The outward–inward growth behavior of microarc oxidation coatings in phosphate and silicate solution. *Mater. Lett.* **2010**, *64*, 2102–2104. [CrossRef]

39. Wei, T.; Yan, F.; Tian, J. Characterization and wear- and corrosion-resistance of microarc oxidation ceramic coatings on aluminum alloy. *J. Alloys Compd.* **2005**, *389*, 169–176. [CrossRef]

40. Tian, J.; Luo, Z.; Qi, S.; Sun, X. Structure and antiwear behavior of micro-arc oxidized coatings on aluminum alloy. *Surf. Coat. Technol.* **2002**, *154*, 1–7. [CrossRef]

41. Sobolev, A.; Kossenko, A.; Borodianskiy, K. Study of the Effect of Current Pulse Frequency on Ti-6Al-4V Alloy Coating Formation by Micro Arc Oxidation. *Materials* **2019**, *12*, 3983. [CrossRef]

42. Koroleva, E.v.; Thompson, G.e.; Hollrigl, G.; Bloeck, M. Surface morphological changes of aluminium alloys in alkaline solution: Effect of second phase material. *Corros. Sci.* **1999**, *41*, 1475–1495. [CrossRef]

43. Mengesha, G.A.; Chu, J.P.; Lou, B.-S.; Lee, J.-W. Corrosion performance of plasma electrolytic oxidation grown oxide coating on pure aluminum: Effect of borax concentration. *J. Mater. Res. Technol.* **2020**, *9*, 8766–8779. [CrossRef]

44. Zhu, Q.; Zhang, B.; Zhao, X.; Wang, B. Binary Additives Enhance Micro Arc Oxidation Coating on 6061Al Alloy with Improved Anti-Corrosion Property. *Coatings* **2020**, *10*, 128. [CrossRef]

45. Su, P.; Wu, X.; Guo, Y.; Jiang, Z. Effects of cathode current density on structure and corrosion resistance of plasma electrolytic oxidation coatings formed on ZK60 Mg alloy. *J. Alloys Compd.* **2009**, *475*, 773–777. [CrossRef]